ASME Journal of Mechanical Design
Online journal at:
https://asmedigitalcollection.asme.org/mechanicaldesign

Topology Design of Compliant Mechanism Design With Multiple Component Modeling Connected by Various Joints

Jun Hwan Kim
School of Mechanical Engineering,
Hanyang University,
Seoul 04763, South Korea
e-mail: junhwan128@gmail.com

Gil Ho Yoon[1]
School of Mechanical Engineering,
Hanyang University,
Seoul 04763, South Korea
e-mail: ghy@hanyang.ac.kr

This study presents a novel framework for the optimal design of compliant mechanisms, specifically addressing the structural drawbacks of conventional single-point or de facto hinges. The hinges often lead to structural instability and stress concentration while deriving maximum motion. To overcome these issues, we introduce a new method that can design stable and elastic domains connected by either revolute or prismatic joints. The new method, called sequential analysis based on the reaction force, can successfully eliminate weak hinge points while optimizing joint locations. The efficiency of developed methodology is validated through several numerical examples, yielding compliant mechanisms with suppressed hinges. [DOI: 10.1115/1.4065459]

Keywords: multi-component topology optimization, hinge-free compliant mechanisms, joint location

1 Introduction

In this study, a novel topology optimization technique designed to maximize displacement is developed in multi-component systems with joint connections. Traditional compliant mechanisms often employ hinge and de facto hinge structures, illustrated in Fig. 1, to facilitate maximum motion. However, these hinges are susceptible to stress concentration, compromising structural integrity. Several prior studies have partially addressed this issue by employing the pseudo-rigid body model (PRBM) to replace hinges with revolute joint, as shown in Fig. 2. To overcome the challenges associated with identifying hinge locations during optimization, the sequential analysis based on the reaction force (SARF) method is proposed. This approach optimizes structural integrity and flexibility by substituting hinges with various joint configurations, thereby reducing stress concentrations. The method has implications for enhancing the durability and functionality of multi-component systems.

Since the inception of topology optimization, various studies have focused on designing compliant mechanisms with flexible hinges, often exploring element-wise stiffness variables. For example, Refs. [1,2] developed methods for maximizing motion in compliant versus rigid-body mechanisms. Stanford and Beran [3] proposed a compliant mechanism to optimize the motion of flapping wings. A comprehensive review paper, Jagtap et al. [4], highlighted diverse applications of compliant mechanisms in various objects like bottle lids, pliers, staplers, etc. The optimization of compliant mechanisms using genetic algorithms was explored using building blocks and actuators in Refs. [5,6]. In Ref. [7], the beam-based compliant mechanisms for both standard and nonstandard compliant mechanism are developed. However, a consistent challenge in these models is the vulnerability of hinges to stress concentrations and large deformations.

The most representative method for replacing hinges is the PRBM, which replaces the flexible hinges with adequate torsional springs in Refs. [8–10]. In Refs. [11,12], the torsion springs are modeled with the PRBM and the deformation trajectories are checked. In Ref. [13], the periodically corrugated hinges are analyzed and replaced with the multiple joints. To design various type of joints, the revolute, spherical, and prismatic joint types are considered to obtain six degrees-of-freedom compliant parallel manipulators in Ref. [14]. The other method is the method to suppress the hinges during the topology optimization procedure. To restrain the hinges in the review paper [15], the hinges are categorized into two types as shown in Fig. 1; one is the one-node hinge, and the other is the de facto hinges. The one-node hinge is the hinge that is only connected to the same nodes, and can be rotated easily. The de facto hinge refers to relatively thin areas where bending occurs, but not at one-node hinges. Because the filtering methods are commonly utilized in compliant mechanism, almost one-node hinges remain to the de facto hinges with additional materials.

Because the one-node hinges can be detected easily compared to the de facto hinges, the studies about one-node hinges are first proposed. In Ref. [16], the hinge-free condition for one-node hinges is implemented to the translation-invariant wavelet shrinkage method. This condition finds the one-node hinge structures and reinforces the one-node hinges with continuous formulation. In Refs. [17,18], the one-node hinges are suppressed with using special finite

[1]Corresponding author.

Contributed by Design Automation Committee of ASME for publication in the Journal of Mechanical Design. Manuscript received December 3, 2023; final manuscript received April 18, 2024; published online May 21, 2024. Assoc. Editor: Shikui Chen.

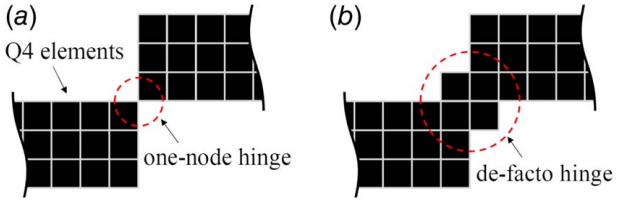

Fig. 1 Schematic figures for (*a*) one-node hinge and (*b*) de facto hinge structures in the conventional compliant mechanism

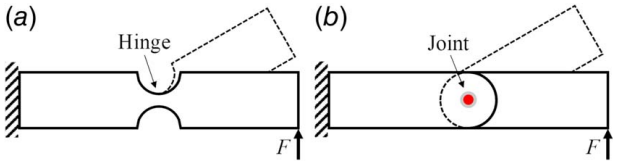

Fig. 2 Illustrative figures for thin hinge and joint structures with deformed shape: (*a*) deformed shape with hinge structure and (*b*) deformed shape with revolute joint structure

elements, one is special triangulation elements and the other is modified quadrilateral elements. Similar to the modified elements, in Ref. [19], the honeycomb discretization method is proposed for hinge-free compliant mechanism. In Ref. [20], morphology-based black and white filters are introduced to make the element densities to zero or one, which can reduce the one-node hinges successively. Various density and sensitivity filtering methods are suggested to avoid the gray elements, which can suppress the one-node hinges, but several de facto hinges are still shown. To avoid both de facto hinges including one-node hinges, various methods are proposed because detecting de facto hinges is difficult compared with the one-node hinge cases. In Ref. [21], both strain energy and mutual strain energy are considered as a multi-objective function to reduce de facto hinges; which are associated with structural stiffness and flexibility respectively. Li and Zhu [22] considered both the maximization of output displacement and the minimization of structural compliance as a multi-objective function in the level-set method. De Leon et al. [23] incorporated the maximum allowable stress as a constraint function to suppress de facto hinges, although it does not completely eliminate de facto hinges. To ensure structural stiffness, Xia and Shi [24] introduced length scale control to guarantee a minimum structural thickness using the skeleton method. As the addressing de facto hinges is important, this study introduces a new approach to both mitigate these hinges and design various joints within multi-component structures.

To mitigate issues related to de facto hinge structures, including one-node hinges, the SARF method is proposed. The SARF method involves separate analyses for multi-component systems, where each component is connected only to joints which are connected to the boundary conditions. Arbitrary unit forces, called SARF forces, are applied at the output nodes of the last (mth) component in the x and y directions. Using finite element analysis, the SARF compliance is computed for each component, and its boundary reaction forces are subsequently computed. The reaction forces are reversed and applied as external forces on the previous (($m-1$)th) component. This process is repeated sequentially for each component back to the first. The sum of all computed SARF compliances is considered as the objective function to be minimized during optimization procedure. This SARF method can increase the stiffness of each component while maintaining the overall motion of the system, effectively suppressing weak hinge structures.

The remainder of this paper is organized as follows. Section 2 outlines topology optimization formulations for single and multi-component models, introducing the SARF method designed to eliminate both hinge and de facto hinge structures. Section 3 validates the proposed method through several numerical examples. The paper concludes with a summary in Sec. 4.

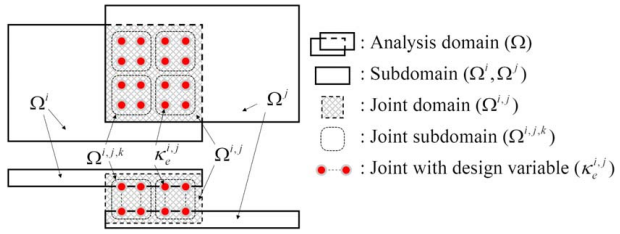

Fig. 3 The definitions of analysis domain, subdomain, joint domain, joint subdomain, and joint design variable for general analysis domain

2 Topology Optimization Formulation for Multi-Component Without Hinge Structure

This section shows the new SARF method for multi-component compliant mechanism with suppressed de facto hinge structures.

2.1 Topology Optimization Formulations for Multi-Component. The topology optimization problem with minimize compliance or maximize output displacement with respect to the volume constraint is formulated. The element stiffness is interpolated based on the solid isotropic material with penalization (SIMP) method for Q4 elements in subdomains and polynomial interpolation function [25] for spring joint elements in joint domains. To determine the equilibrium equation in the analysis domain Ω, the following finite element approach is utilized:

$$\nabla \cdot \boldsymbol{\sigma}(\mathbf{u}) + \mathbf{b} = \mathbf{0} \quad \text{in}\,\Omega, \;\; \boldsymbol{\sigma} = \mathbf{C}\boldsymbol{\varepsilon} \tag{1}$$

where the stress tensor and the displacement field vector are denoted by $\boldsymbol{\sigma}$ and $\mathbf{u}$, respectively. The body force term ($\mathbf{b}$) is neglected in this study. The strain tensor and the constitutive matrix of the structures are denoted by $\boldsymbol{\varepsilon}$ and $\mathbf{C}$, respectively.

The multi-subdomain model is depicted in Fig. 3. The analysis domain Ω is separated and modeled as mth subdomains Ω^i ($i = 1, 2, \ldots, m$) where the number of subdomains is denoted by m. The overlapping area between the ith subdomain Ω^i and jth subdomain Ω^j is defined as the joint domain $\Omega^{i,j}$, as follows:

$$\Omega = \Omega^1 \cup \cdots \Omega^i \cup \Omega^j \cdots \cup \Omega^m, \quad \Omega^i \cap \Omega^j = \Omega^{i,j} \tag{2}$$

The joints, represented by red circle pairs with gray edges, can be defined anywhere within the joint domain area. The joint subdomain $\Omega^{i,j,k}$ is defined as a set of arbitrary shape, capable of encompassing multiple joints. These joint subdomains may overlap with each other and are considered to calculate the joint dispersal (JD) constraint $\varphi^{i,j}$. The JD constraint ensures that the minimum distance between optimized joints is greater than the $\delta_{\min}$ value. Further details on the JD constraint will be discussed later. The global stiffness matrix is obtained by summing the stiffness matrices of both

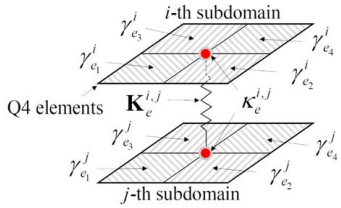

Fig. 4 The definition of zero-length spring joint connecting the *i*th and *j*th subdomains

the subdomain and joint components, as follows:

$$\mathbf{K} = \mathbf{K}_{\text{subdomain}} + \mathbf{K}_{\text{joint}} \tag{3}$$

$$\mathbf{K}_{\text{subdomain}} = \sum_{i=1}^{m} \sum_{e=1}^{N^i} \gamma_e^3 \mathbf{K}_{\text{nominal}}^i \tag{4}$$

where N^i denotes the number of elements in the ith subdomain. The stiffness matrix for the subdomain is computed by summing all the finite elements, using the SIMP method with a penalty value of 3. The nominal stiffness of the subdomain denoted by $\mathbf{K}_{\text{nominal}}$ represents the stiffness matrix for Q4 elements with density of 1.

As illustrated in Fig. 4, the joints consist of the simple zero-length spring element, which connect and transfer the strain energies between each subdomain. The stiffness matrix of a single joint is controlled using the combination of the interpolation function $f(\kappa_e^{i,j})$, the densities of adjacent elements $\gamma_{\text{Adjacent}}^i$ and $\gamma_{\text{Adjacent}}^j$, and the nominal stiffness of the joints $\mathbf{K}_{\text{nominal}}^{i,j}$ in Eq. (5).

$$\mathbf{K}_{\text{joint}} = \sum_{i=1}^{m} \sum_{j=1, i\neq j}^{m} \sum_{e=1}^{N^{i,j}} \mathbf{K}_e^{i,j} \tag{5a}$$

$$\mathbf{K}_e^{i,j} = f(\kappa_e^{i,j}) \gamma_{\text{Adjacent}}^i \gamma_{\text{Adjacent}}^j \mathbf{K}_{\text{nominal}}^{i,j} \tag{5b}$$

where $N^{i,j}$ denotes the number of joint elements in the joint domain $\Omega^{i,j}$. The stiffness values of joint elements are modified using the interpolation function $f(\kappa_e^{i,j})$, which is influenced by the joint design variable $\boldsymbol{\kappa}_e^{i,j}$ in the following Eq. (6).

$$f(\kappa_e^{i,j}) = \frac{(\kappa_e^{i,j})^n}{1 + (1 - (\kappa_e^{i,j})^n) \dfrac{\alpha^{i,j}}{dim}} \tag{6a}$$

$$\begin{aligned} \gamma_{\text{Adjacent}}^i &= \text{mean}(\gamma_{e_1}^i,\ \gamma_{e_2}^i,\ \gamma_{e_3}^i,\ \gamma_{e_4}^i) \\ \gamma_{\text{Adjacent}}^j &= \text{mean}(\gamma_{e_1}^j,\ \gamma_{e_2}^j,\ \gamma_{e_3}^j,\ \gamma_{e_4}^j) \\ \mathbf{K}_{\text{nominal}}^{i,j} &= c\ u_x^i u_y^i u_x^j u_y^j \end{aligned} \tag{6b}$$

$$\mathbf{K}_{\text{nominal}}^{i,j} = \begin{matrix} u_x^i \\ l^{i,j} \\ 0 \\ -l^{i,j} \\ 0 \end{matrix} \begin{matrix} u_y^i \\ 0 \\ l^{i,j} \\ 0 \\ -l^{i,j} \end{matrix} \begin{matrix} u_x^j \\ -l^{i,j} \\ 0 \\ l^{i,j} \\ 0 \end{matrix} \begin{matrix} u_y^j \\ 0 \\ -l^{i,j} \\ 0 \\ l^{i,j} \end{matrix} \tag{6c}$$

$$l^{i,j} = \alpha^{i,j} \times \text{mean}(\text{diag}(\mathbf{K}_{\text{nominal}}^i), \text{diag}(\mathbf{K}_{\text{nominal}}^j)) \tag{6d}$$

The variable *dim* in Eq. (6a) represents the number of dimensions which is two for 2D problem and three for 3D problem. The interpolation function $f(\kappa_e^{i,j})$ has advantage in achieving convergence (0 or 1) for the joint design variables. Using a larger value for maximum stiffness can result in convergence problems during the topology optimization process when the SIMP method is used to compute joint stiffness. For more detailed information on the interpolation function, see Ref. [25]. The adjacent design variables for connected subdomains ($\gamma_{\text{Adjacent}}^i$ and $\gamma_{\text{Adjacent}}^j$) are calculated using the average value of adjacent design variables, as described in Eq. (6b). These adjacent design values ensure that joints disconnected from the subdomains are eliminated. The nominal stiffness matrix term, $\mathbf{K}_{\text{nominal}}^{i,j}$, is calculated using the stiffness matrix for springs in both the x and y directions. The maximum spring stiffness value, $l^{i,j}$, is determined by multiplying the constant $\alpha^{i,j}$ with the diagonal term of the nominal stiffness matrix of the connected subdomains. In this paper, the value of $\alpha^{i,j}$ is set to 10^3 for all numerical examples, indicating that the maximum stiffness of the joints is 10^3 times greater than the stiffness of the subdomains.

Because the stiffness in both the x and y directions for the joints is identical and sufficiently strong, the joints can behave as revolute joints. These revolute joints can be transformed into prismatic joints (single-degree-of-freedom kinematic pairs) by making minor adjustments to the stiffness ratio between the x and y directions, as follows:

$$\mathbf{K}_{\text{nominal}}^{i,j} = \begin{matrix} u_x^i \\ l_x^{i,j} \\ 0 \\ -l_x^{i,j} \\ 0 \end{matrix} \begin{matrix} u_y^i \\ 0 \\ l_y^{i,j} \\ 0 \\ -l_y^{i,j} \end{matrix} \begin{matrix} u_x^j \\ -l_x^{i,j} \\ 0 \\ l_x^{i,j} \\ 0 \end{matrix} \begin{matrix} u_y^j \\ 0 \\ -l_y^{i,j} \\ 0 \\ l_y^{i,j} \end{matrix} \tag{7a}$$

$$\begin{aligned} l_x^{i,j} &= \alpha_x^{i,j} \times \text{mean}(\text{diag}(\mathbf{K}_{\text{nominal}}^i), \text{diag}(\mathbf{K}_{\text{nominal}}^j)) \\ l_y^{i,j} &= \alpha_y^{i,j} \times \text{mean}(\text{diag}(\mathbf{K}_{\text{nominal}}^i), \text{diag}(\mathbf{K}_{\text{nominal}}^j)) \end{aligned} \tag{7b}$$

In the equations above, the values $\alpha_x^{i,j}$ and $\alpha_y^{i,j}$ represent the stiffness multiplier in the x and y directions for the joints, respectively. When $\alpha_x^{i,j}$ is sufficiently smaller than $\alpha_y^{i,j}$, the joint behaves as a y-directional prismatic joint, allowing sliding along the y-axis. The application and solution involving these prismatic joints will be discussed in Sec. 3.

The joints connecting subdomains are predefined in the post-processing process. The location of these joints remains invariant throughout the optimization process, although the stiffness of each joint can be adjusted by the joint design variable. Joints are considered disconnected if their stiffness value is zero (or close to zero). On the contrary, joints with a sufficiently high stiffness value are considered revolute or prismatic joints. Consequently, changing the joint design variables can influence the determination of the optimized joint locations.

For applying the multi-component modeling to the compliant mechanism scheme, the topology optimization formulation for single- and multi-subdomain cases is defined separately. In the conventional compliant mechanism scheme for single-subdomain case, the topology optimization problem can be formulated as follows:

$$\begin{aligned} \underset{\boldsymbol{\gamma}}{\text{Maximize}} \quad & u_{\text{out}} = \mathbf{L}^{\text{T}}\mathbf{U} \\ \text{Subject to}: \quad & \\ & V(\boldsymbol{\gamma}) \le V_0 \\ & \mathbf{KU} = \mathbf{F} \\ & 0 < \gamma_{\min} \le \boldsymbol{\gamma} \end{aligned} \tag{8}$$

In case of the conventional compliant mechanism for single subdomain in Eq. (8), the output displacement u_{out} is considered as the objective function and maximized subject to a volume constraint V. The objective vector $\mathbf{L}$ is configured with value of 1 at the output degrees-of-freedom, while all other components are set to zero. The optimization formulation described above is applicable only to the single-subdomain case. For multi-subdomain scenario, the optimization formulation is defined as follows:

$$\begin{aligned} \underset{\mathbf{x}}{\text{Minimize}} \quad & C_{\text{SARF}} = \textstyle\sum_{i=1}^{m} C_{\text{SARF}}^i \\ \text{Subject to}: \quad & \\ & |u_{\text{out}}| \ge u_{\text{target}} \\ & \varphi^{i,j} \le 0 \\ & \textstyle\sum_{i=1}^{m} V^i(\boldsymbol{\gamma}) \le V_0 \\ & \mathbf{KU} = \mathbf{F} \\ & \mathbf{x} = [\boldsymbol{\gamma},\ \boldsymbol{\kappa}] \\ & 0 < \gamma_{\min} \le \boldsymbol{\gamma} \le 1, \quad 0 \le \boldsymbol{\kappa} \le 1 \\ & i,\ j = 1,\ 2, \ldots,\ m, \quad i \neq j \end{aligned} \tag{9}$$

In the multi-subdomain optimization formulation in Eq. (9), unlike the single-subdomain cases, the summation of the SARF compliance value C_{SARF} is considered as objective function and is minimized. The detailed information for SARF compliance will be discussed in Sec. 2.2. In the single-subdomain case described in Eq. (8), the objective function u_{out} is now considered as the

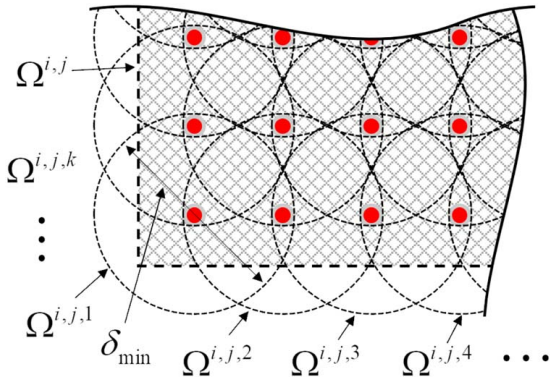

Fig. 5 The definition of the circle-shaped joint subdomains to implement the JD constraint

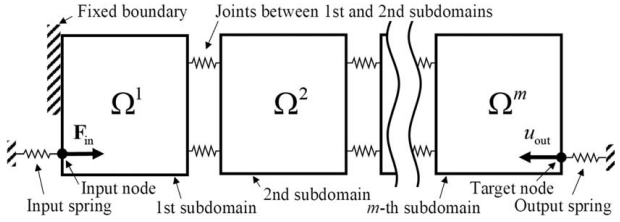

Fig. 6 Definition of multi-subdomain model for compliant mechanism. *m* subdomains are connected sequentially with joints to calculate the output displacement.

displacement constraint, which must exceed the target displacement value u_{target}. Achieving a lower SARF compliance value tends to result in a structure with suppressed hinges. But, selecting a specific reference value for SARF compliance is challenging, because it is highly dependent on the shape and characteristics of the model. Therefore, in the case of multiple subdomains, SARF compliance is considered as the objective function, while the output displacement u_{out} is treated as a constraint. The target displacement value u_{target} can be obtained from the objective function with single subdomain as described in Eq. (8). Minimizing the SARF compliance value subject to the output displacement constraint aims to achieve the desired output displacement while suppressing hinge structures.

The JD constraint, denoted as $\varphi^{i,j}$, is implemented to the multi-subdomain optimization problem, which ensures that the minimum distance between each joint is greater than a specified value, $\delta_{\min}$. This JD constraint is applied to permit a maximum of one joint within each joint subdomain. The enforcement of this one joint condition is mathematically represented in Eq. (10*a*), which involves the summation of joint design variables minus the maximum joint design value in each joint subdomain $\Omega^{i,j,k}$. To adapt the maximum function for numerical computation, it is implemented as a p-norm with a sufficiently large p-value (specifically, $p_1 = 20$). The JD constraint value, $\varphi^{i,j}$, is defined using additional p-norm function with $p_2 = 6$ as shown in Eq. (10*b*), effectively ensuring that only one joint remains within each joint subdomain. To extend this principle to maintain a minimum distance between each joint, every joint subdomain is defined as circles with a diameter of $\delta_{\min}$, centered on all joints, as illustrated in Fig. 5. If the one joint condition in Eq. (10*a*) is satisfied across all joint subdomains, it guarantees that the minimum distance between topological joints greater than $\delta_{\min}$. This constraint is crucial in preventing the clustering of joints in small area, thereby aiding in managing the structural complexity. For a more comprehensive understanding of the JD constraint, please refer to Ref. [26].

$$\varphi^{i,j,k} = \sum_{\kappa_e \in \Omega^{i,j,k}} \kappa_e - \left[\sum_{\kappa_e \in \Omega^{i,j,k}} (\kappa_e)^{p_1} \right]^{\frac{1}{p_1}} \leq 0 \qquad (10a)$$

$$\varphi^{i,j} = \left[\sum_{k=1}^{N_{i,j}} \left(\varphi^{i,j,k}\right)^{p_2} \right]^{\frac{1}{p_2}} - 10^{-5} \leq 0 \qquad (10b)$$

The volume constraint $\sum_{i=1}^{m} V^i$ for multi-subdomains limits the total volume of all subdomains. Since the constraint is applied to the volume summation rather than each individual subdomain, the volume ratio among the subdomains can change during the optimization process. The design variable set $\mathbf{x}$ contains the subdomain design variable $\boldsymbol{\gamma}$ and the joint design variable $\boldsymbol{\kappa}$. Those variables affect the element stiffness matrices for the quad elements and joint elements, respectively.

In this study, the optimization problems are solved in two steps. First, a single-subdomain optimization is conducted to get the maximum output displacement value, which can be a reference value for the target displacement value in the next multi-subdomain problem. The first step is essential to define the baseline of output displacement for multi-subdomain problems, where the primary goal of this study is to suppress hinge structures using the SARF compliance as the objective function. Although minimizing the SARF compliance increases structural stiffness, it might reduce output displacement, hence a displacement constraint is applied as constraint. Moreover, this approach allows to compare the deformation patterns of de facto hinges and joint structures. Since they are

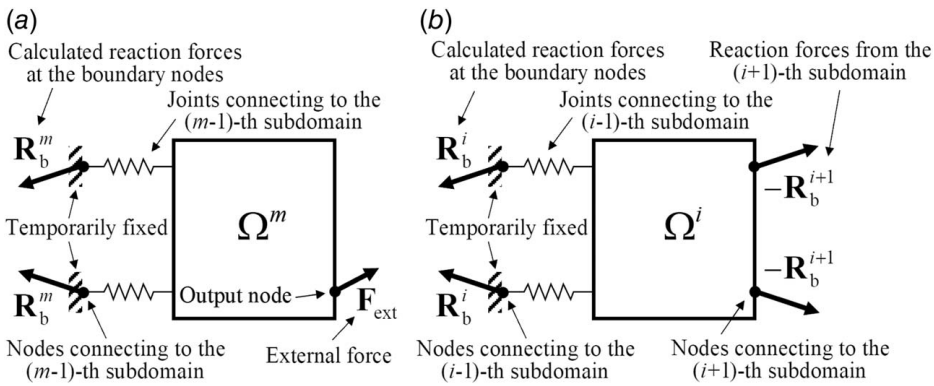

Fig. 7 Definitions of the SARF multi-subdomain model for calculating the SARF compliance value: (*a*) in the last *m*th subdomain, external forces are applied to calculate the reaction forces at the connected subdomain and (*b*) the calculated reaction forces, when reversed in direction, are considered as the external forces in the *i*th subdomain ($i < m$)

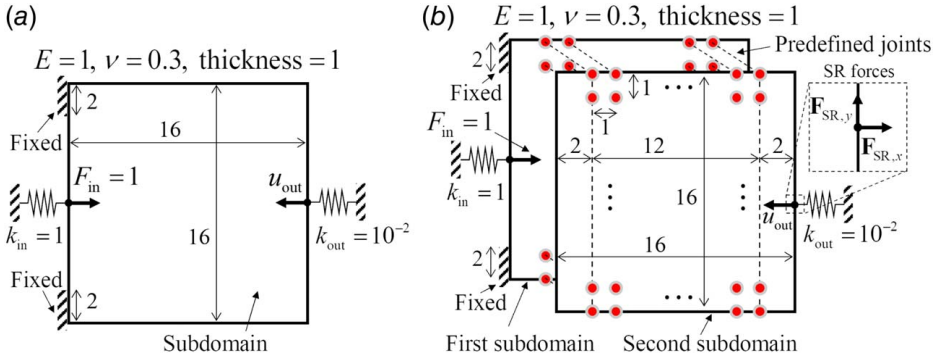

Fig. 8 Example 1: the design domains for displacement inverter problem with (*a*) single subdomain and (*b*) multi subdomain. The joints do not exist in the single subdomain, while 13 × 17 joints are predefined in the multi-subdomain problem. The SARF forces are applied at the output node in the multi-subdomain problem.

expected to be similar, the first step is crucial for verifying the accuracy of the joint locations in the optimized model.

2.2 Compliant Mechanism With Suppressed Hinge Structure. In this section, the new multi-subdomain model for SARF method is defined to calculate the SARF compliance value in Eq. (9), aiming to suppress hinge structures. As stated in the previous section, the analytical model is modeled in two different ways and is analyzed separately for each. First, all subdomains are assumed to be connected sequentially with spring joints, as described in Fig. 6. In this multi-subdomain model, the output displacement u_{out} is calculated using the input force F_{in}, which is same as the compliant mechanism. Second, the subdomains are separated from each other and solved using the external forces, starting from the mth subdomain down to the first subdomain, as described in Fig. 7. In Fig. 7(*a*), the joints between the $(m-1)$th and mth subdomains are connected to the mth subdomain with temporarily fixed boundary condition, and the external forces (F_{ext}) are applied to the output node. The external forces at the mth subdomain are defined as unit forces in the x and y directions. After finishing the calculation of the reaction force at the mth subdomain, the reversed reaction forces are now considered as the external forces for the $(m-1)$th subdomain (Fig. 7(*b*)). Those sequential analysis processes are repeated one by one until the first subdomain. The SARF compliance value is calculated using those method in Fig. 7. A lower SARF compliance value indicates that the stiffness values of each subdomain are increasing, suppressing the formation of hinge structures. Since the SARF compliance value is calculated using only the separated subdomains and connected joints, the overall stiffness of the model shown in Fig. 6 may be lower due to these joint connections. These can achieve an optimized shape with both free-hinge structures and revolute joints, resulting in a high u_{out} value. Because the two different analytical method is conducted simultaneously during the optimization process, all parameters are independent from each other, except for the design variables $\boldsymbol{\gamma}$ and $\boldsymbol{\kappa}$. Therefore, the unit forces in the x and y directions are chosen for the external force to calculate the SARF compliance value. The SARF compliance value and the global stiffness equation in the ith subdomain can be defined as follows:

$$C_{SARF} = \sum_{i=1}^{m} C^i_{SARF} \tag{11a}$$

$$C^i_{SARF} = \left(\mathbf{F}^i_R\right)^T \mathbf{U}^i_R \tag{11b}$$

$$\mathbf{K}^i_R \mathbf{U}^i_R = \mathbf{F}^i_R \tag{12a}$$

$$\mathbf{K}^i_R = \begin{bmatrix} \mathbf{K}^i_{R,bb} & \mathbf{K}^i_{R,bf} \\ \mathbf{K}^i_{R,fb} & \mathbf{K}^i_{R,ff} \end{bmatrix}, \quad \mathbf{U}^i_R = \begin{bmatrix} \mathbf{U}^i_{R,b} \\ \mathbf{U}^i_{R,f} \end{bmatrix}, \quad \mathbf{F}^i_R = \begin{bmatrix} \mathbf{F}^i_{R,b} \\ \mathbf{F}^i_{R,f} \end{bmatrix} \tag{12b}$$

From the above formula, C_{SARF} is the summation of the SARF compliance of all subdomains. The subscript R and superscript i in Eq. (11*b*) indicate values corresponding to the ith subdomain, as shown in Fig. 7. The degrees-of-freedom in the global stiffness Eq. (12*a*) can be divided into those that correspond to the temporarily fixed boundary conditions (indicated by the subscript b) and the remaining free parts (indicated by the subscript f) in Eq. (12*b*). Due to the boundary condition, the displacement vector ($\mathbf{U}^i_{R,b}$) and the force vector ($\mathbf{F}^i_{R,b}$) are zero vectors. As a result, the SARF compliance value from Eq. (11*b*) and the global stiffness equation from Eq. (12*a*) can be rewritten as follows:

$$C^i_{SARF} = \left(\mathbf{F}^i_{R,f}\right)^T \mathbf{U}^i_{R,f} \tag{13}$$

$$\mathbf{K}^i_{R,ff} \mathbf{U}^i_{R,f} = \mathbf{F}^i_{R,f} \tag{14}$$

And the reaction force vector ($\mathbf{R}^i_b$) at the boundary degrees-of-freedom can be expressed using the submatrix of the stiffness matrix as follows:

$$\mathbf{R}^i_b = \mathbf{K}^i_{R,bf} \mathbf{U}^i_{R,f} \tag{15}$$

The force vector ($\mathbf{F}^i_{R,f}$) for the ith subdomain can be defined as the reversed reaction force vector.

$$\mathbf{F}^i_{R,f} = \begin{cases} -\mathbf{R}^{i+1}_b & \text{if } i < m \\ \mathbf{F}_{ext} & \text{if } i = m \end{cases} \tag{16}$$

To apply the SARF compliance value in the optimization process, differentiating Eqs. (11*b*) and (16) with respect to the design variables yields the following expressions:

$$\frac{\partial C^i_{SARF}}{\partial \mathbf{x}} = \frac{\partial \left(\mathbf{F}^i_{R,f}\right)^T}{\partial \mathbf{x}} \mathbf{U}^i_{R,f} - \left(\mathbf{U}^i_{R,f}\right)^T \frac{\partial \mathbf{K}^i_{R,ff}}{\partial \mathbf{x}} \mathbf{U}^i_{R,f} \tag{17}$$

$$\frac{\partial \mathbf{F}^i_{R,f}}{\partial \mathbf{x}} = \begin{cases} -\frac{\partial \mathbf{R}^{i+1}_b}{\partial \mathbf{x}} & \text{if } i < m \\ \mathbf{0} & \text{if } i = m \end{cases} \tag{18}$$

Calculating the derivative of $\mathbf{F}^i_{R,f}$ in Eq. (17) is highly challenging since the force vector is a function of the design variables. As shown in Eq. (16), the force vector $\mathbf{F}^i_{R,f}$ can be categorized based

on whether $i < m$ or $i = m$. Since external force vector $\mathbf{F}_{\text{ext}}$ is independent of the design variables, the derivative of $\mathbf{F}^i_{\text{R,f}}$ can be expressed as shown in Eq. (18). To differentiate $\mathbf{R}^{i+1}_{\text{b}}$, substituting $i+1$ for the superscript i and applying the Lagrange multiplier, $\boldsymbol{\lambda}^{i+1}$ with Eq. (14), Eq. (15) can be rewritten as follows:

$$\mathbf{R}^{i+1}_{\text{b}} = \mathbf{K}^{i+1}_{\text{R,bf}}\mathbf{U}^{i+1}_{\text{R,f}} + \boldsymbol{\lambda}^{i+1}\left(\mathbf{K}^{i+1}_{\text{R,ff}}\mathbf{U}^{i+1}_{\text{R,f}} - \mathbf{F}^{i+1}_{\text{R,f}}\right) \tag{19}$$

After differentiating the above equation with respect to the design variables, and substituting $-\mathbf{K}^{i+1}_{\text{R,bf}}\left(\mathbf{K}^{i+1}_{\text{R,ff}}\right)^{-1}$ for $\boldsymbol{\lambda}^{i+1}$ to eliminate the derivative terms of $\mathbf{U}^{i+1}_{\text{R,f}}$, the equation can be simplified as follows:

$$\frac{\partial \mathbf{R}^{i+1}_{\text{b}}}{\partial \mathbf{x}} = \frac{\partial \mathbf{K}^{i+1}_{\text{R,bf}}}{\partial \mathbf{x}}\mathbf{U}^{i+1}_{\text{R,f}} + \mathbf{K}^{i+1}_{\text{R,bf}}\left(\mathbf{K}^{i+1}_{\text{R,ff}}\right)^{-1} \times \left(\frac{\partial \mathbf{F}^{i+1}_{\text{R,f}}}{\partial \mathbf{x}} - \frac{\partial \mathbf{K}^{i+1}_{\text{R,ff}}}{\partial \mathbf{x}}\mathbf{U}^{i+1}_{\text{R,f}}\right) \tag{20}$$

As shown in above equation, the derivative term of reaction force $\mathbf{R}^{i+1}_{\text{b}}$ can be expressed in terms of the derivative term of $\mathbf{F}^{i+1}_{\text{R,f}}$. By substituting the above equation into Eq. (18) for the case of $i < m$, the derivative term of $\mathbf{F}^i_{\text{R,f}}$ can be expressed in terms of the derivative term of $\mathbf{F}^{i+1}_{\text{R,f}}$. Starting with the zero vector for the derivative of $\mathbf{F}^m_{\text{R,f}}$, the derivative term of $\mathbf{F}^i_{\text{R,f}}$ can be calculated sequentially from $i = m$ down to $i = 1$.

Due to the computational intensity and time-consuming nature of directly calculating the inverse of $\mathbf{K}^{i+1}_{\text{R,ff}}$ in Eq. (20), it is common to use matrix decomposition techniques that efficiently solve linear equation. Using matrix decomposition techniques, the inverse of $\mathbf{K}^{i+1}_{\text{R,ff}}$ can be efficiently calculated via $\mathbf{K}_{\text{R,bf}}$. Specifically, for $i = 1$ (the first subdomain), the computational time for $\mathbf{K}^{i+1}_{\text{R,bf}}\left(\mathbf{K}^{i+1}_{\text{R,ff}}\right)^{-1}$ can be reduced by pre-multiplying $\mathbf{U}_{\text{R,f}}$ from Eq. (17) with $\mathbf{K}_{\text{R,bf}}$. This reduces the dimensions of the matrix from $\text{b} \times \text{f}$ to $1 \times \text{f}$, thereby accelerating the time required for computing the inverse matrix.

3 Numerical Examples

To show the validity of the SARF method in topology optimization for multiple components connected by joints, this section solves several optimization problems. The analysis domain is divided into several subdomains connected by zero-length joints and it is intended to make the subdomains stiffer without hinge but with joint. Joints causing actuation for compliant mechanism are modeled by the zero-length spring elements. The SARF forces (F_{SARF}) are applied at the output displacement nodes in the last subdomain, i.e., the mth subdomain for the topology optimization for mechanism with m components. The forces defined at the x and y directions are applied for the calculation of each compliance and the minimization of the summation of the compliance is considered as the objective function. Indeed, we would like to emphasize that through this approach the components become stiffer without hinge but with joints. The material properties are set to the same values for all examples, i.e., 1 for elastic modulus and 0.3 for Poisson's ratio. Four nodes quad elements with plane stress and eight nodes brick elements are implemented in 2D and 3D problems, respectively. To address the well-known checkerboard problem in topology optimization, a sensitivity filter has been applied across all numerical examples. For 2D problems, the filtering distance is set to 1.6× the element size, while for 3D problems, a distance of 1.75× the element size is utilized, both exceeding the diagonal length of each element. While the sensitivity filter comes with challenges such as ambiguous and non-smooth boundaries. Numerous studies have introduced to relax these issues in topology optimization, such as the density filter with a heaviside function [27], the moving morphable component approach [28], and the level-set method [29], among others. However, given that this study focuses on suppressing de facto hinges, which are relatively thin structures, methods to address the non-smooth boundary phenomenon have not been considered. The method of moving asymptotes is implemented as an optimization algorithm [30].

3.1 Example 1: Displacement Inverter. The displacement inverter problem is first considered in Fig. 8. In Fig. 8(*a*), the single-subdomain design is considered as a reference design for the displacement inverter problem, which the output displacement (u_{out}) is maximized. On the other hand, in Fig. 8(*b*), the multiple subdomains are considered with 221 predefined joints. Similar to the single-subdomain problem, the fixed boundary condition, the input node, and the input spring are applied only at the first subdomain, while the output spring is connected to the second subdomain. As mentioned, the force of magnitude 1 is applied to the output node in the x and y directions. In the multiple subdomain case, the SARF compliance value is considered as an objective function with the output displacement and joint dispersal constraints. The input and output springs modeling the stiffness of a workpiece are connected to the input and output nodes with spring stiffness of 1 and 10^{-2} respectively. The 30% of volume fraction is considered in both problems. Through the topology optimization, it is beneficial that the number of the hinges is determined by the optimization algorithm in addition to the layouts. It is our intention to control the location and number of hinges. From an engineering point of view, the hinge or joint structures have some importance in additive manufacturing with the size limitation.

3.1.1 Topology Optimization With Single Subdomain. To show the effect of the developed method, the single-subdomain problem in Fig. 8(*a*) is first considered. The maximization of the output displacement (u_{out}) is pursued by topology optimization. The optimization results are shown in Fig. 9 with the optimized layout, deformed shape (displacement scale of 1), and the von-mises stress distribution. As noted, some de facto hinges appear randomly denoted by the red dotted circles; it is possible to manually interpret them in realization.

It is observed that the optimized von-mises stresses are concentrated in the four locations, where the boundary points, the input node, and the hinge structures. The maximum von-mises stress value (1.288×10^{-1}) appeared near the input node, while the

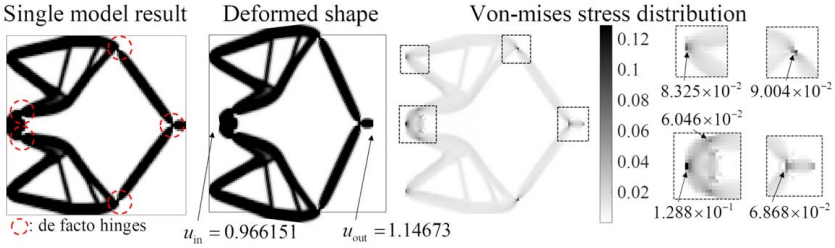

Fig. 9 The optimized layout and the von-mises stress distribution for the single-subdomain displacement inverter problem (the displacement scale of the deformed shape: 1)

Table 1 Resultant strain energy values for displacement inverter with single-subdomain problem in Fig. 9

Type	$\frac{1}{2}F_{\text{in}}u_{\text{in}}$	$\frac{1}{2}k_{\text{in}}u_{\text{in}}^2$	$\frac{1}{2}k_{\text{out}}u_{\text{out}}^2$	$\frac{1}{2}\sum_{e}^{\text{model}}\mathbf{U}_e^{\text{T}}\mathbf{K}_e\mathbf{U}_e$	$\frac{1}{2}\sum_{e}^{\text{joint}}\mathbf{U}_e^{\text{T}}\mathbf{K}_e\mathbf{U}_e$
Value	0.4831	0.4667	6.575×10^{-3}	9.776×10^{-3}	N/A
Ratio (%)	100	96.615	1.361	2.024	N/A

stress values near the hinge structures (9.004×10^{-2} and 6.868×10^{-2}) are also nonphysically high. It is possible to reduce those stress concentrations by eliminating the thin hinge or joint structure. The strain energies are calculated to check the energy transfer between the input and the output nodes in Table 1. The summation of deformed energies including both input/output spring ($(1/2)k_{\text{in}}u_{\text{in}}^2$, $(1/2)k_{\text{out}}u_{\text{out}}^2$) and the model/joint deformation ($(1/2)\sum_e^{\text{model}}\mathbf{U}_e^{\text{T}}\mathbf{K}_e\mathbf{U}_e$, $(1/2)\sum_e^{\text{joint}}\mathbf{U}_e^{\text{T}}\mathbf{K}_e\mathbf{U}_e$) is exactly same as the input energy value ($(1/2)F_{\text{in}}u_{\text{in}}$). The most of the input energy is used for deformation of the input spring, which is 4.667×10^{-1} (96.615% of the input energy). Only 4.667×10^{-1} (1.361% of the input energy) is transferred to deform the output spring. The deformation of the subdomain part only consumes the strain energy about 9.776×10^{-3} (2.024% of the input energy) resulting in the output displacement of 1.1467. These values are treated as the reference value for comparison with the following examples.

To suppress that hinge structure and the non-physical stress distributions, the SARF method is applied compared with the target displacement constraint condition using the Fig. 8(*b*). The optimization formulation in Eq. (9) is implemented at the multi-subdomain problem. The SARF compliance value is minimized and considered as an objective function, and the output displacement value (u_{out}) is implemented as a constraint function which is greater than specific target displacement value (u_{target}). All other optimization parameters except the target displacement value are set as the same values. With the present optimization scheme, the optimization results in Fig. 10 can be obtained. The u_{target} values are set as 0.8, 1.0, 1.14673, and 1.2 in Figs. 10(*a*)–10(*d*) respectively. In Fig. 10(*c*), the u_{target} value of 1.14673 is the optimized output displacement from the single-subdomain result. To compare the von-mises stress distribution, the von-mises stress for Fig. 10(*c*) is shown in Fig. 11 which the u_{out} value is same as the single-subdomain

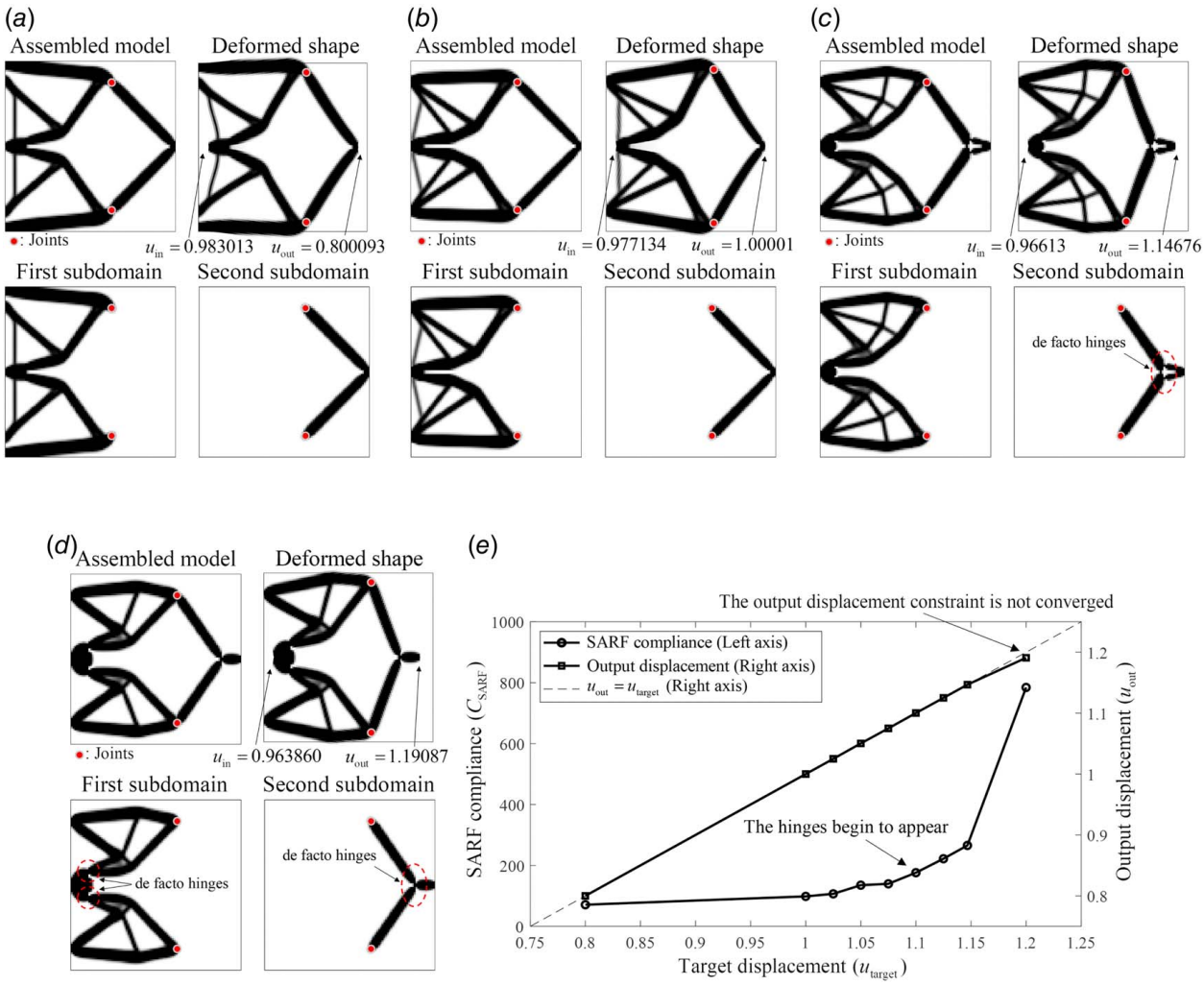

Fig. 10 Hinge-free multi-subdomain topology optimization results for minimizing SARF compliance value. The output displacement constraint values (u_{target}) are set as (*a*) 0.8, (*b*) 1.0, (*c*) 1.14673, (*d*) 1.2, and (*e*) the responses with respect to the target displacement. The minimum joint distance value (δ_{min}) is set as 4. The scale factor for deformed shape is set as 1.

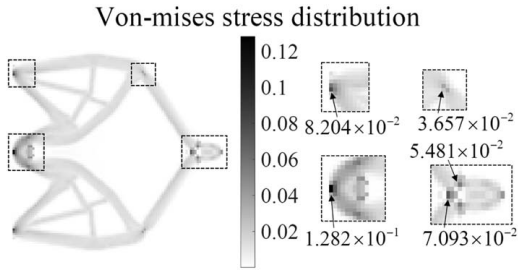

Fig. 11 The von-mises stress distribution with multi-subdomain problem in Fig. 10(*c*)

result. The von-mises stress distributions for other cases are illustrated in the Appendix. The followings are what we find out:

- In Figs. 10(*a*) and 10(*b*), it is observed that the two joints are optimized in the de facto hinge locations in the single-subdomain result in Fig. 9, and the de facto hinges are eliminated in the optimized shapes with the uniform thickness bar shapes.
- Because the joints are modeled with a zero-length spring elements, the optimized joints are deformed as rotational pin joints similar to the conventional hinge structures. The minimization of the SARF compliance makes the stiffness of each subdomain stronger, while the target displacement constraint makes the stiffness of the assembled model weaker. Due to these contradictory two conditions, the hinges in each model are suppressed and the role of the conventional hinges is supplanted by the joints in the optimization process.
- As the optimization results, the u_{out} values are converged to the u_{target} values. As the u_{target} values increases from 0.8 to 1.0, the height of the optimized shape near the boundary condition is reduced to converge the increased u_{target} values with same input force F_{in}.
- In the case of the larger u_{target} values in Figs. 10(*c*) and 10(*d*), the optimization results are significantly changed as follows. Almost hinge structures are suppressed around the optimized joint location, but some de facto hinges are not eradicated around the input force node and output node denoted as the dotted red circles. And the case of the u_{target} is 1.2, the optimized output displacement is converged as 1.19087 which violates the displacement constraint.
- In the case of the same u_{out} value in single- and multi-subdomain cases, the two de facto hinge structures are replaced by two-pin joint structures. This makes the von-mises stress distribution around the joint (3.657×10^{-2} in Fig. 11) is decreased about 59.38% compared with the stress value around the hinge structure (9.004×10^{-2} in Fig. 9). The decreased stress has the advantage for the stress failure and fatigue life.

The minimization of the SARF compliance try to make the de facto hinge structure suppressed, however, some de facto hinges are not eradicated around the input force node and output node denoted as the dotted red circles. The remaining hinge structures can be explained by the following two reasons. The first reason is that the target displacement constraint values are set as too large value, leading to infeasible region to suppress the hinge structures. Additionally in the second reason, in order to get rid of the hinge, the SARF compliance must be smaller. As illustrated in Fig. 10(*e*), hinge structures begin to appear when the target displacement value reaches 1.1. It is important to note that the SARF compliance value does not change significantly as the hinges appear. Although SARF compliance generally increases as the target displacement value rises, there is a nearly flat region between 1.05 and 1.075, where no hinge structures are observed. The specific threshold value for completely suppressing hinge structures is not clearly defined and may vary across different optimization models.

The joint domain is intentionally positioned between two subdomains with a specific offset from the boundary conditions and the output node. This configuration prevents the second subdomain from being directly connected to the boundary conditions and the output node from being connected to the first subdomain. To evaluate the effect of these offsets, the multi-subdomain model with the extended joint domain is optimized, as illustrated in Fig. 12. In this model, 17×17 predefined joints connect the first and second subdomains. All optimization parameters are identical to those used in the multi-subdomain optimization result shown in Fig. 10(*b*). With this extended joint subdomain, the optimized result is shown, where the second subdomain is essentially empty, and only one joint is optimized at the output node. The optimized shape is similar to the result in the single optimization result, while the de facto hinge structures are shown. To avoid such local optima in multi-subdomain optimization, joints are placed with some spacing from both the boundary condition and the output node in all examples.

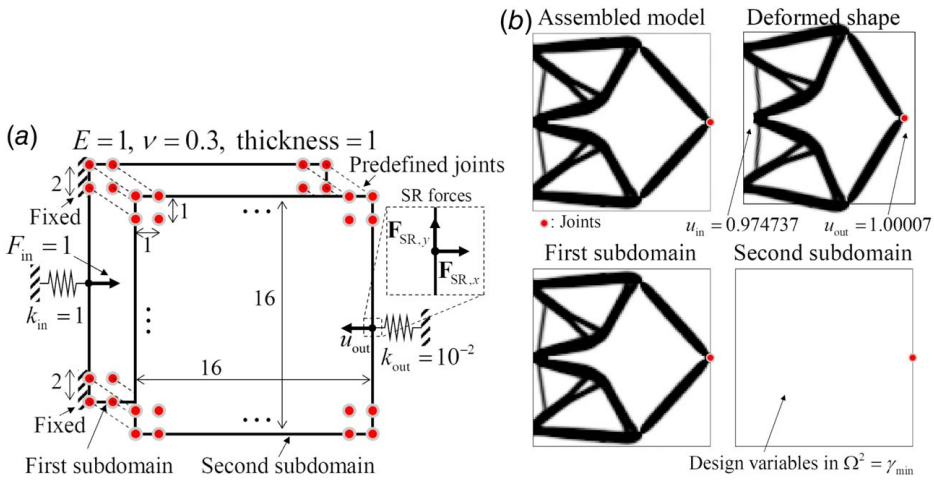

Fig. 12 Multi-subdomain topology optimization result with an extended joint domain area that extends to the boundary conditions and output nodes: (*a*) model definition and (*b*) corresponding optimized result are shown, respectively. Except for the joint domain, all optimization parameters remain consistent with those in Fig. 10(*b*). In the second subdomain, all optimized design variables converge to the value γ_{min}.

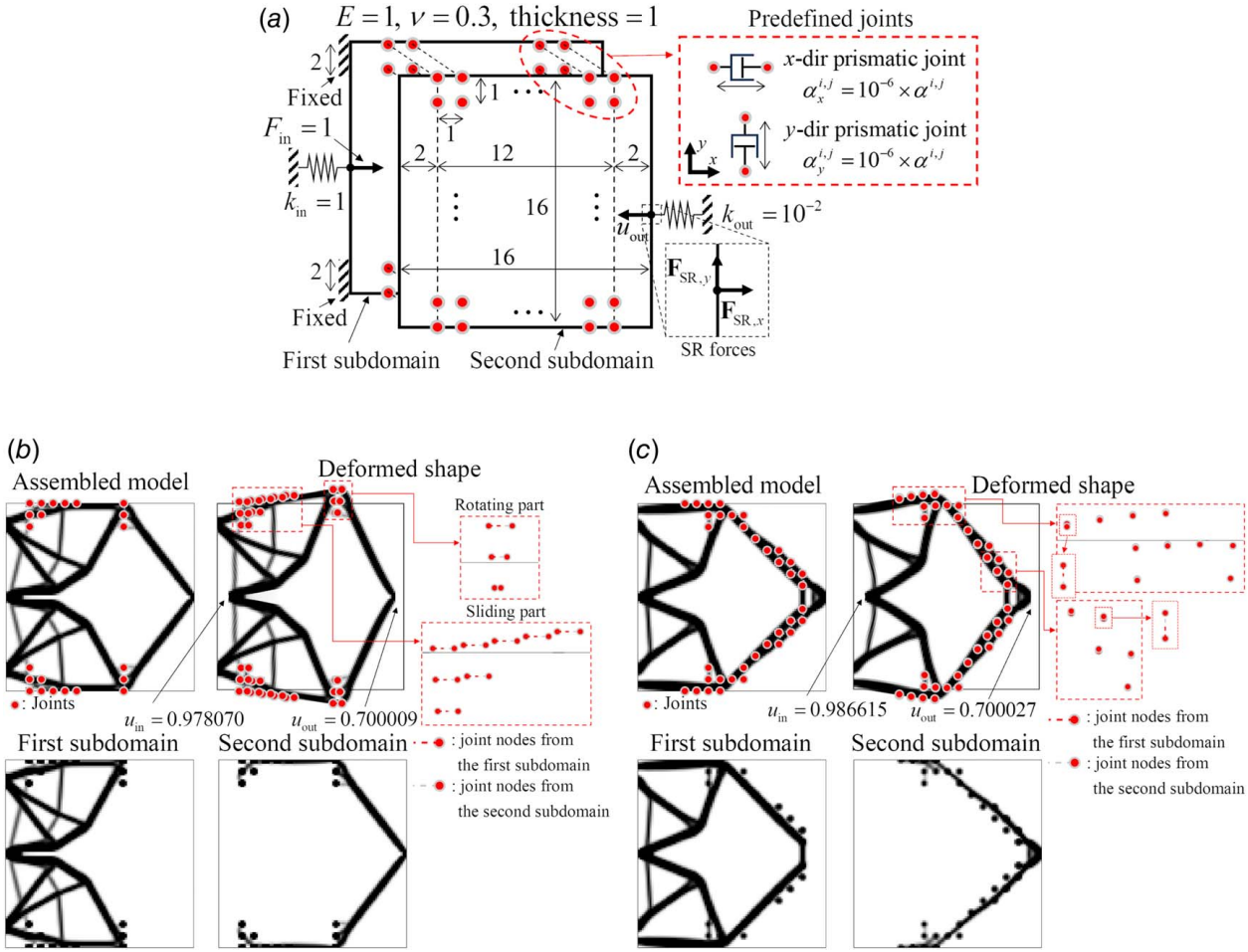

Fig. 13 Example 1 results with prismatic joint: (*a*) the problem definition, optimized layouts with the prismatic joints sliding in the (*b*) *x*-direction and (c) *y*-direction

3.1.2 Topology Optimization With the SARF Method With Prismatic Joint. As stated, the present SARF method has the advantage in designing compliant part and joint part, simultaneously. To show the potential application of the present development, this subsection considers the topology optimization with continuum structure and prismatic joint simultaneously. The engineering problem considered in this subsection is set as topology optimization for compliant mechanism with prismatic joint. For the sake of illustration, only the prismatic joint allowing the sliding in the *x*-direction or *y*-direction is considered in Fig. 13(*a*). To implement the prismatic joints, the values of the joint stiffness multipliers ($\alpha_x^{i,j}$ and $\alpha_y^{i,j}$) in the sliding direction are set to 10^{-6} times the value in the perpendicular direction in Eq. (7). The target displacement values at output nodes in both cases are set as $u_{\text{out}} = 0.7$, and the other optimization parameters and the optimization algorithms are set as the same except the joint stiffness multiplier.

In Fig. 13(*b*), the prismatic joint allowing sliding in the *x*-direction is considered and optimized. The first and the second subdomains are optimized as shown in the bottom of Fig. 13(*b*). The prismatic joints in the *x*-direction appear at the sliding joint part (left-top and left-bottom) and at the rotating joint part (center-top and center-bottom) marked with the dashed red box. The investigation of the motions of the prismatic joints at the sliding joint part reveals that the prismatic joints mainly allow the sliding in the *x*-direction. In the two prismatic joints at the rotating joint part, the relative displacement in the top side joint is larger than the relative displacement in the bottom-side joint, which results in the relative rotation. With these relative motions, the optimized shape differs from that of the revolute joint case shown in Fig. 10(*a*). This is because the prismatic joints in Fig. 13(*b*) are unable to resist the input force directed along the *x*-axis. In Fig. 13(*c*), the prismatic joints sliding in the *y*-direction are optimized. The optimized

Table 2 Resultant strain energy values for displacement inverter problem with the *x*-direction (Fig. 13(*b*)) and *y*-direction (Fig. 13(c)) prismatic joints

Case	Type	$\frac{1}{2}F_{\text{in}}u_{\text{in}}$	$\frac{1}{2}k_{\text{in}}u_{\text{in}}^2$	$\frac{1}{2}k_{\text{out}}u_{\text{out}}^2$	$\frac{1}{2}\sum_e^{\text{model}}\mathbf{U}_e^{\text{T}}\mathbf{K}_e\mathbf{U}_e$	$\frac{1}{2}\sum_e^{\text{joint}}\mathbf{U}_e^{\text{T}}\mathbf{K}_e\mathbf{U}_e$
x-dir	Value	0.4890	0.4783	2.450×10^{-3}	5.892×10^{-3}	2.382×10^{-3}
	Ratio (%)	100	97.807	0.501	1.205	0.487
y-dir	Value	0.4933	0.4867	2.450×10^{-3}	4.132×10^{-3}	2.030×10^{-5}
	Ratio (%)	100	98.662	0.497	0.838	4.116×10^{-3}

Table 3 Resultant strain energy values for displacement inverter with multi-subdomain problems in Fig. 10

Case (u_{target})	Type	$\frac{1}{2}F_{in}u_{in}$	$\frac{1}{2}k_{in}u_{in}^2$	$\frac{1}{2}k_{out}u_{out}^2$	$\frac{1}{2}\sum_e^{model}\mathbf{U}_e^T\mathbf{K}_e\mathbf{U}_e$	$\frac{1}{2}\sum_e^{joint}\mathbf{U}_e^T\mathbf{K}_e\mathbf{U}_e$
0.8	Value	0.4915	0.4832	3.200×10^{-3}	5.149×10^{-3}	7.263×10^{-8}
	Ratio (%)	100	98.301	0.651	1.048	1.478×10^{-5}
1.0	Value	0.4886	0.4774	5.000×10^{-3}	6.172×10^{-3}	1.095×10^{-7}
	Ratio (%)	100	97.713	1.023	1.263	2.241×10^{-5}
1.1467	Value	0.4831	0.4667	6.575×10^{-3}	9.784×10^{-3}	2.184×10^{-7}
	Ratio (%)	100	96.613	1.361	2.203	4.520×10^{-5}
1.2	Value	0.4819	0.4645	7.091×10^{-3}	1.033×10^{-2}	2.261×10^{-7}
	Ratio (%)	100	96.386	1.471	2.143	4.692×10^{-5}

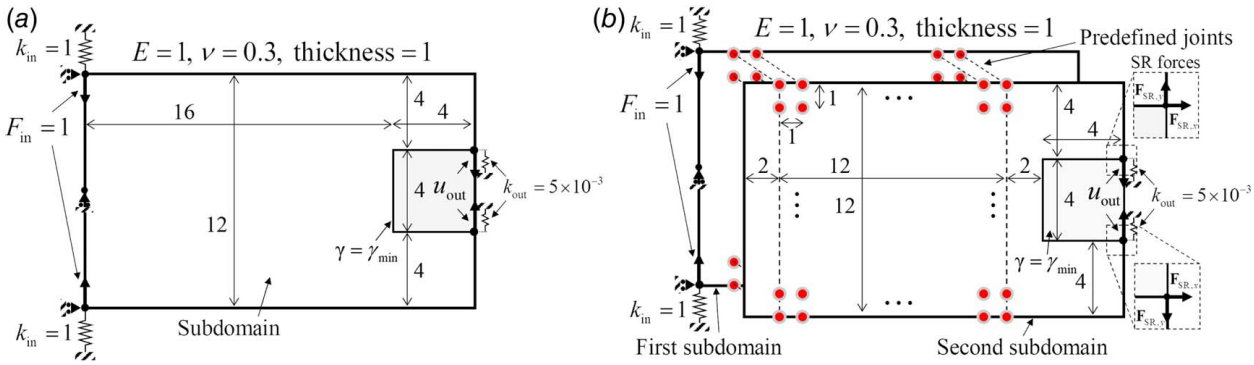

Fig. 14 Example 2: the design domains for gripper problem with (*a*) single subdomain and (*b*) multi subdomain. The joints do not exist in the single subdomain, while 13 × 13 joints are predefined in the multi-subdomain problem. The SARF forces are applied to the output nodes in the multi-subdomain problem.

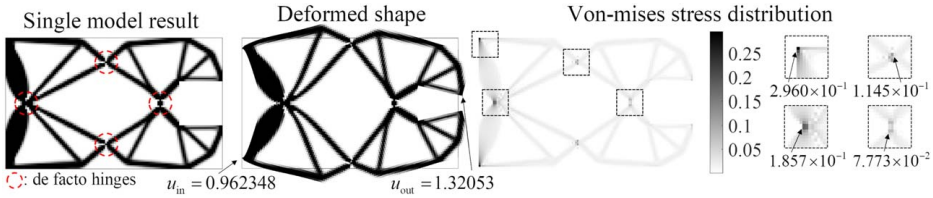

Fig. 15 The optimized layout and von-mises stress distribution for the single-subdomain gripper problem without SARF method. The displacement scale of the deformed shape is 1.

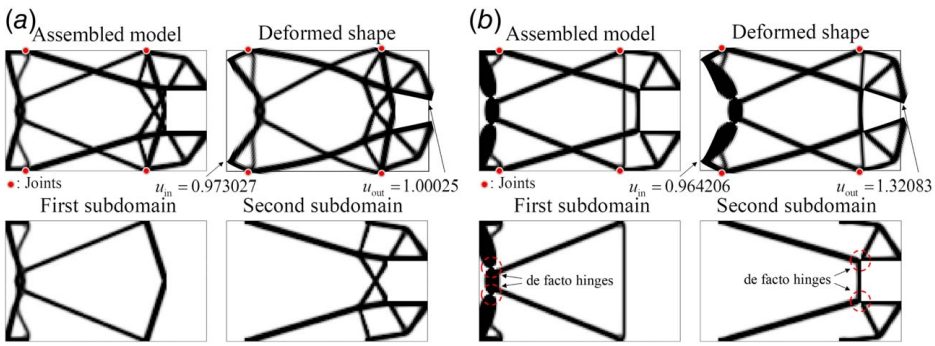

Fig. 16 Hinge-free multi-subdomain topology optimization result for minimizing SARF compliance value with u_{target} changes. The u_{target} is set as (*a*) 1.0 and (*b*) 1.32053 respectively. The minimum joint distance value (δ_{min}) is set as 4. The scale factor for deformed shape is set as 1.

prismatic joints are concentrated in a narrow area between the first and second subdomains with given condition to minimize the objective function. Compared to the *x*-direction prismatic joint result, the joints work as sliding in the *y*-direction. But, the detailed locations of the prismatic joints before and after the actuation show that the significant displacements do not occur. The optimized shape closely resembles the revolute joint scenario depicted in Fig. 10(*a*). A significant number of optimized joints are tightly clustered between the first and second subdomains, ensuring that the output displacement constraint is satisfied.

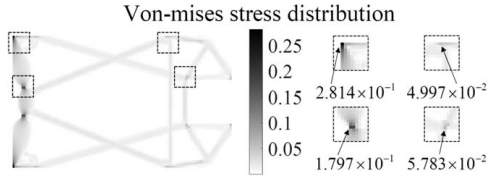

Fig. 17 The von-mises stress distribution with multi-subdomain problem in Fig. 10(*b*)

The resultant strain energy values with prismatic joints are shown in Table 2. When comparing these results from the perspective of the strain energy, some differences can be found in the joint domain area. In the *x*-direction prismatic joint case, the strain energy ratio of the joint domain is greatly increased compared with Table 3. Because all joints in the second subdomains are deformed in the right direction, the *x*-directional deformation of joints is large enough and the strain energy is increased. Therefore, it is crucial to ensure that the E_x value should not be decreased excessively to maintain numerical stability. If the E_x is set as very small value, the numerical stability will be decreased. On the other hand, the deformation of joints with the *y*-direction prismatic joint is quite small compared with the *x*-direction prismatic joint case. Because the joints are optimized closed to the output node, the *y*-directional deformation of joints are relatively small, thus exhibiting small strain energy value in joint domain. Although it may also be possible to optimize the direction of prismatic joint to maximize the output displacement value, it is not pursued here as the purpose of the present study is to show the concept of the SARF method.

3.2 Example 2: Gripper. For the next example, the gripper design in topology optimization is considered in this subsection. The problem definitions for single and multi subdomain including the material properties and the geometry are given in Fig. 14. The output displacements in the $\pm y$ directions are calculated at the two output nodes in the right corner nodes. The design variables in 4×4 area are set to non-design area with minimum density, $\gamma_{\min}$. The unit forces in the $\pm y$ directions are applied to the input nodes with input spring with stiffness of 1, while the output springs with stiffness of 5×10^{-3} are attached to the output

Table 4 Resultant strain energy for single subdomain (Fig. 15) and multi-subdomain (Fig. 16) problems

Case	Type	$\frac{1}{2}F_{\text{in}}u_{\text{in}}$	$\frac{1}{2}k_{\text{in}}u_{\text{in}}^2$	$\frac{1}{2}k_{\text{out}}u_{\text{out}}^2$	$\frac{1}{2}\sum_e^{\text{model}}\mathbf{U}_e^{\text{T}}\mathbf{K}_e\mathbf{U}_e$	$\frac{1}{2}\sum_e^{\text{joint}}\mathbf{U}_e^{\text{T}}\mathbf{K}_e\mathbf{U}_e$
Single	Value	0.9623	0.9261	8.719×10^{-3}	2.752×10^{-2}	N/A
	Ratio (%)	100	96.235	0.906	2.859	N/A
Multi (1.0)	Value	0.9730	0.9468	5.003×10^{-3}	2.124×10^{-2}	2.410×10^{-7}
	Ratio (%)	100	97.303	0.514	2.183	2.477×10^{-5}
Multi (1.32053)	Value	0.9642	0.9297	8.723×10^{-3}	2.579×10^{-2}	2.396×10^{-7}
	Ratio (%)	100	96.420	0.905	2.675	2.485×10^{-5}

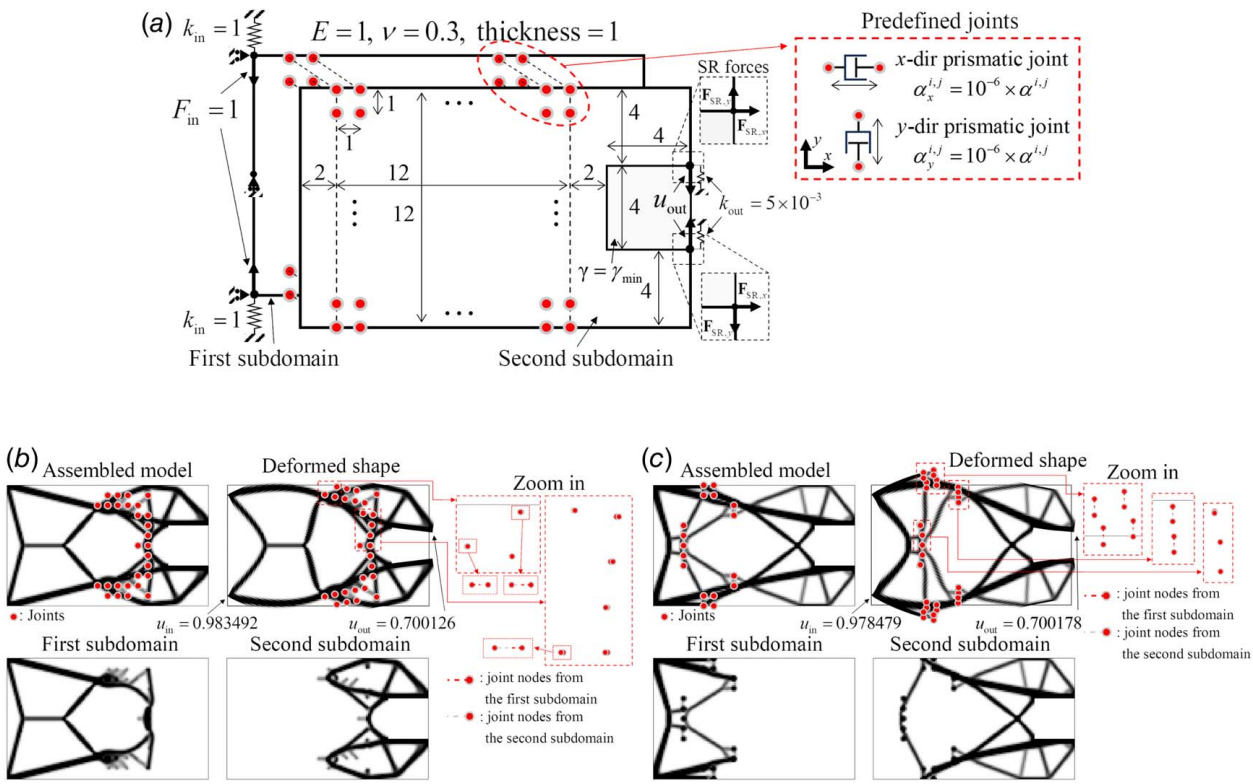

Fig. 18 Example 2 results with the prismatic joints: (*a*) the problem definition, optimized layouts with the prismatic joints sliding in the (*b*) *x*-direction and (c) *y*-direction

Table 5 Resultant strain energy values for gripper problem with the *x*-direction (Fig. 18(*b*)) and *y*-direction (Fig. 18(*c*)) prismatic joints

Case	Type	$\frac{1}{2}F_{\text{in}}u_{\text{in}}$	$\frac{1}{2}k_{\text{in}}u_{\text{in}}^2$	$\frac{1}{2}k_{\text{out}}u_{\text{out}}^2$	$\frac{1}{2}\sum_e^{\text{model}}\mathbf{U}_e^{\text{T}}\mathbf{K}_e\mathbf{U}_e$	$\frac{1}{2}\sum_e^{\text{joint}}\mathbf{U}_e^{\text{T}}\mathbf{K}_e\mathbf{U}_e$
x-dir	Value	0.9835	0.9673	2.451×10^{-3}	1.378×10^{-2}	6.878×10^{-6}
	Ratio (%)	100	98.349	0.249	1.401	6.993×10^{-4}
y-dir	Value	0.9785	0.9574	2.451×10^{-3}	1.776×10^{-2}	8.496×10^{-4}
	Ratio (%)	100	97.848	0.251	1.815	8.683×10^{-2}

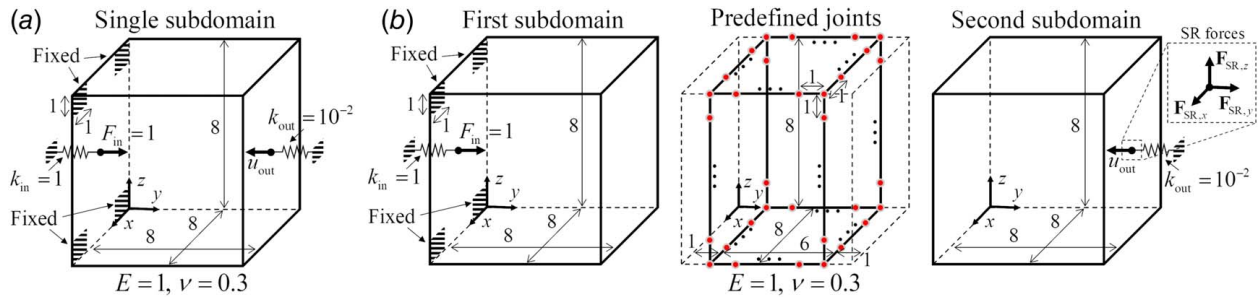

Fig. 19 Example 3: the design domains for 3D displacement inverter problem with (*a*) single subdomain and (*b*) multi subdomains ($9\times7\times9$ joints with interval and the SARF force defined each subdomains)

nodes. To avoid the singularity error during optimization process, the displacement of y is fixed in the single left-center node, which does not affect to the deformation of the compliant mechanism because of the symmetrical shape of subdomain. The 169 revolute joints are predefined and the SARF forces are applied in the $+x$ and $\pm y$ directions at the output nodes only at the multiple subdomain problem.

An optimization gripper layout and its von-mises distribution with a single subdomain are shown in Fig. 15. As observed in the first example, several de facto hinge structures denoted by the red dotted circles can be found with output displacement of 1.32053 and the hinge structures play a crucial role in maximizing output displacement utilizing the flexibility of the hinge. In addition, the von-mises stress values are highly concentrated around the hinge structures and the boundaries. To control the hinge structures suppressed, the minimizing SARF compliance with target displacement of 1.0 with multi subdomain problem in Eq. (9) is optimized with four revolute joints in Fig. 16(*a*). The designs in the first and the second subdomains with the revolute joints are free from the hinges and the compliant substructures can be designed successfully. Unlike the single-subdomain problem with some hinges, thin and elongated structures are interconnected to suppress any hinge structure. When the target displacement value is set identically to the output displacement of the single subdomain result, the four revolute joints with similar location are optimized and four hinges occur, as depicted in Fig. 16(*b*). The optimized shape with large target displacement value($u_{\text{target}}=1.32053$) is considerably similar compared to the optimized shape with lower value ($u_{\text{target}}=1.0$), but the stiffness of the optimized structure is weaker to make large output displacement. The resultant von-mises stress distribution in multi-subdomain problem with identical output displacement is illustrated in Fig. 17. Although the concentrated von-mises stress values closed to the input forces and the left-center hinge structures are not significantly decreased, the stress value near the hinge is dramatically decreased. The strain energy distribution for single and multi subdomain is given in Table 4. Similar to the previous displacement inverter problem, most of the input energy is used to deform the input spring and less then 1% of energy is transferred through the output spring. The sum of the strain energy in the joints is negligibly small value, which indicates that the joints perform as ideal revolute joints.

As stated in the previous example, the optimization using the SARF method can be extended to the prismatic joint in the x and y directions, i.e., prismatic joints. As shown in Fig. 18(*a*), the optimization parameters, except for the joint stiffness, are identical to those for revolute joints problem in Fig. 14(*b*). The target displacement value is set as 0.7 at the output nodes. The optimized results using the x- and y-directional prismatic joint can be found in Figs. 18(*b*) and 18(*c*) respectively. The structural stiffness values connecting the prismatic joints are being reduced to minimize the deformation of the prismatic joints in both problems. Therefore, the sliding deformations of joints depicted in Fig. 18(*b*) are relatively small, and the most deformations are transferred through the joint stiffness in the y-direction. Contrary to the optimized results with prismatic joints in the x-direction, the sliding deformations of the joints are obvious with prismatic joints in the y-direction. In the two optimization results using the prismatic joints, no distinct

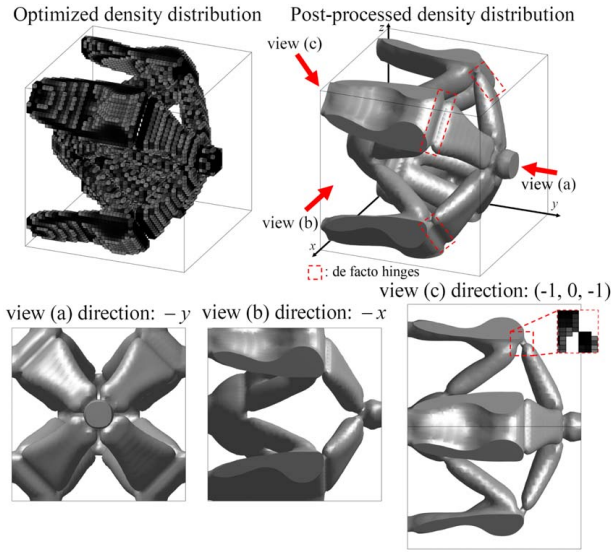

Fig. 20 The optimized layout for the single subdomain 3D displacement inverter problem without the SARF method. Elements with density below 0.5 are excluded in the density distribution. The isosurface with density 0.4 is considered to post-processed figure. The input and output displacement values are 0.967010 and 1.08563 respectively.

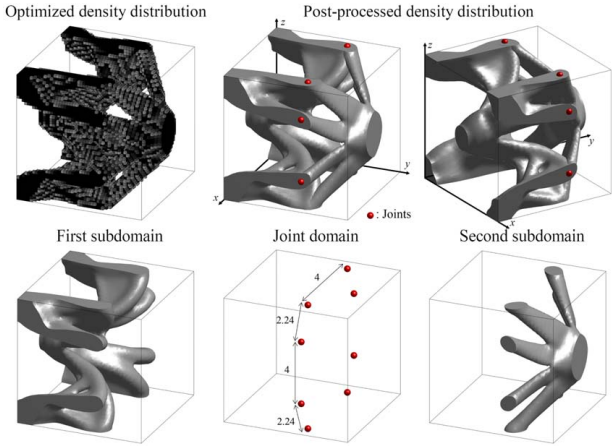

Fig. 21 The hinge-free optimized layout for multi-subdomain optimization with minimizing the SARF compliance value (the target displacement constraint u_{target}: 0.8, the minimum joint distance value (δ_{min}): 2, the input displacement: 0.979099, the output displacement: 0.800013)

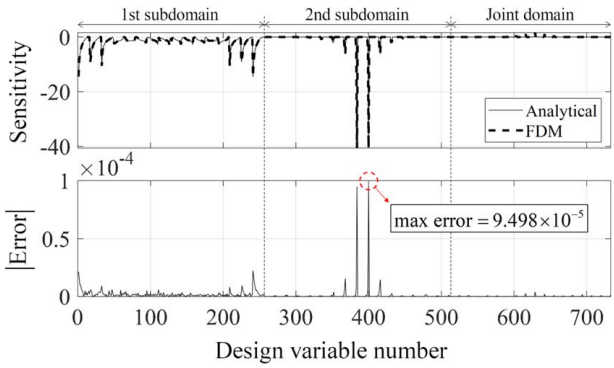

Fig. 22 Sensitivity analysis result for the objective value (C_{SARF}) with respect to design variables (x) in example 1 with coarse mesh

hinge structures are observed, excluding the areas with weaker stiffness near the joints. The optimized strain energy distributions are summarized in Table 5. Due to the minor joint deformations in the prismatic joint problem in the x-direction, the total strain energy in the joint domain is negligibly small compared to that in the prismatic joint problem in the y-direction. Due to the greater sliding occurring at the prismatic joint in the x-direction, the strain energy of the subdomain is increased to satisfy the same target displacement constraint.

3.3 Example 3: Displacement Inverter in 3D. As the final example, the 3D displacement problem with higher degrees-of-freedom to verify the applicability of the present SARF method. In Fig. 19,$8 \times 8 \times 8$ cubic-shape analysis domain is discretized by $48 \times 48 \times 48$ brick elements. Similar to the displacement inverter problem in the example 1, the input force of magnitude 1, denoted as F_{in}, is applied in $+y$-direction at the center of the left side. The $-y$-direction output displacement, denoted as u_{out}, is computed at the center of the right side. The input and output springs are connected at the input node and output node, with the stiffness of 1 and 0.01 respectively. Four fixed boundary conditions of size 1×1 are applied to the corner of the left side. The 567 spring joints are predefined at the joint domain of size $8 \times 6 \times 8$ with interval of 1, and operates as spherical joints in the multi-subdomain problem. The SARF forces with the x, y, and z directions are applied at the output nodes to minimize the SARF compliance values. The 20% of volume fraction is considered in both problems, and the JD constraint with distance of 2 is considered in multiple subdomain problem. The numbers of freedom are 352,947 and 705,894 for single- and multi-subdomain problem respectively.

First of all, in the single-subdomain results in Fig. 20 is optimized using Fig. 19(*a*), which results with the four linear-shape de facto hinges marked by the red circles. To straightforwardly check the density distribution, the element with density below 0.5 (elements with low stiffness) are omitted in the figure showing optimized density distribution figure. The figure is refined by depicting the post-processed density distribution using an isosurface with 0.5 density level. It is important to note that this post-processed density distribution is only used for visualization purposes and not for finite element analysis. The three figures with different view directions are shown in bottom three figures. The output displacement reaches to 1.0856 with 0.9670 for the input displacement.

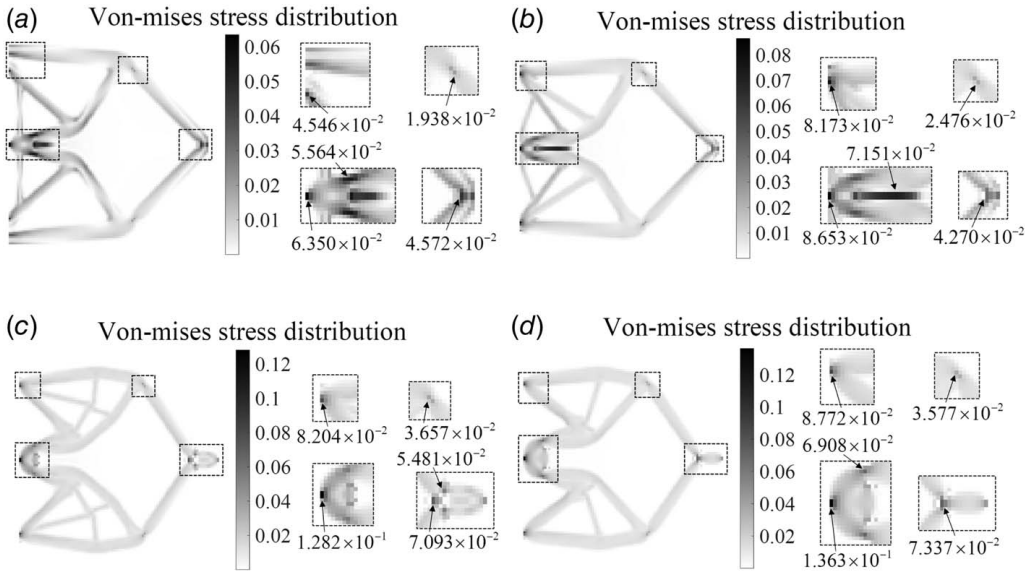

Fig. 23 The von-mises stress distributions for assembled model in Fig. 10. The concentrated stress values are denoted in the bottom-side figures: (*a*) $u_{target} = 0.8$, (*b*) $u_{target} = 1.0$, (*c*) $u_{target} = 1.14673$, and (*d*) $u_{target} = 1.2$.

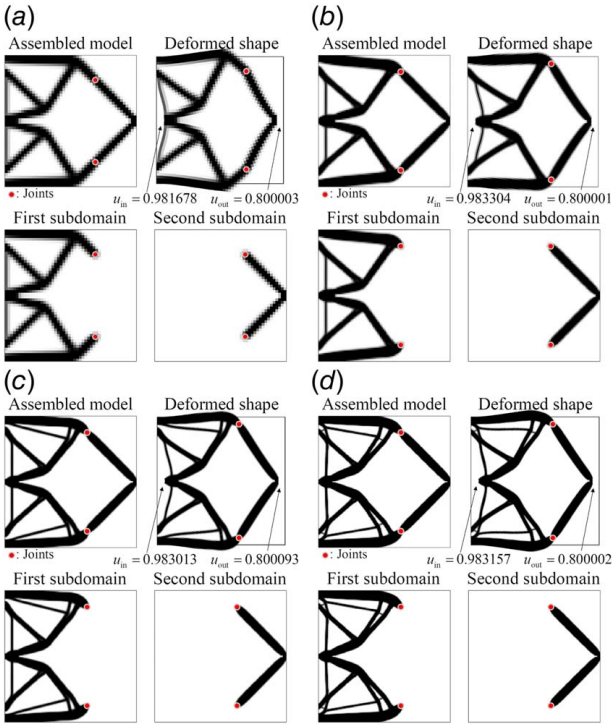

Fig. 24 Topology optimization results for different mesh discretizations with suppressed hinge structure. The output displacement constraint value is set as 0.8, and all optimization parameters, except the mesh size, remain identical to those in Fig. 10(*a*). The total numbers of degrees-of-freedom are: (*a*) 9604, (*b*) 37,636, (*c*) 84,100, and (*d*) 148,996.

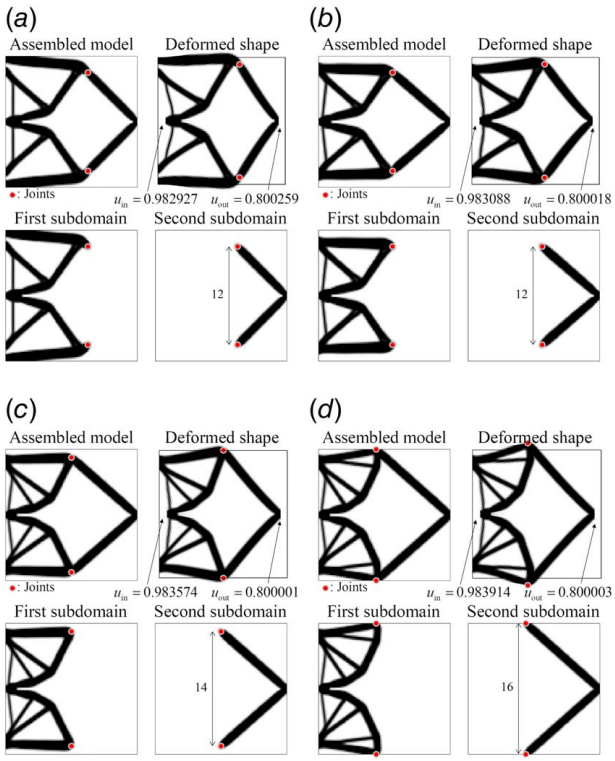

Fig. 25 Topology optimization results for different minimum joint distance value. The output displacement constraint value is set as 0.8, and all optimization parameters, except the δ_{min} value, remain identical to those in Fig. 10(*a*). The minimum joint distance values are set as (*a*) 8, (*b*) 12, (*c*) 14, and (*d*) 16.

To suppress de facto hinge structures, the multi-subdomain problem in Fig. 19(*b*) is considered. The target displacement value is set as 0.8, and the minimum distance of the JD constraint is set as 2 at the multi-subdomain problem. As shown in Fig. 21, the hinge-free optimized layout with two subdomains is derived with eight joints. In the optimized density distribution figure (left-top) in Fig. 21, the elements with density below 0.5 are excluded in optimized density distribution figure, and the isosurface with density 0.5 level is shown in the other post-processed density distribution figures. The eight optimized joints with the minimum distance of 2.24 are connecting between the first and the second subdomains, and the de facto hinges are successfully eradicated. The optimized output displacement is 0.800013 with 0.979099 for the input displacement. Note that the output displacement value is decreased compared to the single result as the hinge structures are removed and replaced with the joint elements. Unlike the prior 2D problem, the elements overlapping around the joints ar optimized; such overlap is physically untenable. The joint stiffness matrix relies on adjacent densities from the connected subdomains, thereby precluding the removal of elements around the joints in both the first and second subdomains. These phenomena are anticipated and will be considered at future research.

4 Conclusions

This study describes the compliant mechanism with suppressed hinge using multicomponent and joint connectivity. One unified flexible component is designed by the topology optimization framework for compliant mechanism. To maximize the motion, often some unphysical features such as the checkerboard, thin structure, and the hinge are often obtained. A few studies understanding their features and roles have been carried out and many innovative approaches have been proposed. Based on the present study, it is our new finding that this issue becomes serious for compliant mechanism design for multiple components. As more than two compliant structures are considered for the compliant mechanism design for multiple components connected by the real joints, i.e., not only the low pair joint but also high pair joint, the unphysical features are frequently observed. To resolve this, the present study develops a new approach called the SARF method setting the sum of the compliance values of each components. In this approach, the reaction forces through joins are defined and the artificial compliance values for each component are computed and considered in the optimization formulation. In addition, the present SARF method bears the benefit that the optimal location and the type of joints can be designed in multiple components. In the present study, not only revolute joint but also prismatic joint can be considered and optimized. For future research, it would be beneficial to develop a new numerical approach capable of incorporating the additive manufacturing characteristics or another manufacturing characteristics.

Acknowledgment

This work was supported by Korea Institute of Energy Technology Evaluation and Planning (KETEP) grant funded by the Korea government (MOTIE) (20202020800030, Development of Smart Hybrid Envelope Systems for Zero Energy Buildings through Holistic Performance Test and Evaluation Methods and Fields Verifications).

Conflict of Interest

There are no conflicts of interest.

Data Availability Statement

The datasets generated and supporting the findings of this article are obtainable from the corresponding author upon reasonable request.

Appendix A: Sensitivity Analysis for SARF Compliance

The sensitivity analysis of SARF compliance is conducted using a displacement inverter example, as illustrated in the model shown in Fig. 8(*b*). In the sensitivity analysis, 16×16 coarse meshes and 13×17 joints are used for two subdomains and joint subdomain respectively. The initial density values are set to 0.5. All the other parameters are set as same value in Fig. 10(*a*). The analytical sensitivity is calculated using Eq. (17) for the design variables, while the sensitivity according to the finite difference method (FDM) is numerically computed with a Δx value of 10^{-6}. The results of the sensitivity analysis for both the subdomains and the joint domain are presented in Fig. 22, and the absolute error values between the analytical and FDM are negligibly small with the maximum error value of 9.498×10^{-5}.

Appendix B: Von-Mises Stress Analysis for Various Target Displacement Values

The von-mises stress distributions from the multi-subdomain displacement inverter example in Fig. 10 are shown in Fig. 23. With an increase in the target displacement value, there is a corresponding increase in the concentration of von-mises stress values. However, these stress values remain lower compared to the von-mises stress concentration observed in the single-subdomain problem depicted in Fig. 9.

Appendix C: The Effect of the Mesh Discretization for Displacement Inverter Example

The impact of mesh discretization on the developed method is evaluated using different mesh sizes, as shown in Fig. 24. The multi-subdomain displacement inverter problem depicted in Fig. 10(*a*) is considered as the baseline model. All optimization parameters remained consistent with this baseline model, except for variations in mesh size. Specifically, the mesh size was doubled in Fig. 24(*a*), multiplied by a factor of 1/1.5 in Fig. 24(*c*), and halved in Fig. 24(*d*). Note that the optimized result presented in Fig. 24(*b*) corresponds to the same model as the baseline model depicted in Fig. 10(*a*). As the number of degrees-of-freedom increases, there are small changes with small and thin branches in optimized shapes. However, the optimized joint locations remain consistent across all cases, except for the case in Fig. 24(*a*). This demonstrates that, through the application of the developed method, de facto hinge structures are effectively suppressed regardless of the mesh discretization.

Appendix D: The Effect of the Joint Dispersal Constraint for Displacement Inverter Example

In displacement inverter problem in Fig. 10(*a*), the minimum joint distance value from the JD constraint is set as 4 while the distance between two optimized joints is 12. The JD constraint does not impact to Fig. 10(*a*) problem. To show the effect of the JD constraint to the hinge-free compliance mechanism, the JD constraint value is increased from 8 to 16, as illustrated in Fig. 25. As the joint distance value increases, the minimum distance between two optimized joints increases, except that the $\boldsymbol{\delta}_{\min}$ is 8. Although the minimum joint distance is increased to 8, the optimized result is almost identical to the optimized result in Fig. 10(*a*).

References

[1] Sigmund, O., 1997, "On the Design of Compliant Mechanisms Using Topology Optimization," J. Struct. Mech., **25**(4), pp. 493–524.

[2] Frecker, M. I., Ananthasuresh, G. K., Nishiwaki, S., Kikuchi, N., and Kota, S., 1997, "Topological Synthesis of Compliant Mechanisms Using Multi-criteria Optimization," ASME J. Mech. Des., **119**(2), pp. 238–245.

[3] Stanford, B., and Beran, P., 2011, "Conceptual Design of Compliant Mechanisms for Flapping Wings With Topology Optimization," AIAA J., **49**(4), pp. 855–867.

[4] Jagtap, S. P., Deshmukh, B. B., and Pardeshi, S., 2021, "Applications of Compliant Mechanism in Today's World – A Review," J. Phys.: Conf. Ser., **1969**(1), p. 012013.

[5] Bernardoni, P., Bidaud, P., Bidard, C., and Gosselin, F., 2004, "A New Compliant Mechanism Design Methodology Based on Flexible Building Blocks," Smart Structures and Materials 2004: Modeling, Signal Processing, and Control, San Diego, CA, Mar. 15–18, SPIE, pp. 244–254.

[6] Gallego, J. A., and Herder, J., 2009, "Synthesis Methods in Compliant Mechanisms: An Overview," International Design Engineering Technical Conferences and Computers and Information in Engineering Conference, San Diego, CA, Aug. 30–Sept. 2, Vol. 49040, pp. 193–214.

[7] Bilancia, P., and Berselli, G., 2021, "An Overview of Procedures and Tools for Designing Nonstandard Beam-Based Compliant Mechanisms," Comput.-Aid. Des., **134**, p. 103001.

[8] Howell, L. L., 2013, "Compliant Mechanisms," 21st Century Kinematics: The 2012 NSF Workshop, Chicago, IL, Aug. 11–12, Springer, pp. 189–216.

[9] Lobontiu, N., 2002, *Compliant Mechanisms: Design of Flexure Hinges*, CRC Press, Boca Raton, FL.

[10] Howell, L. L., Magleby, S. P., and Olsen, B. M., 2013, *Handbook of Compliant Mechanisms*, John Wiley & Sons, Hoboken, NJ.

[11] Pei, X., Yu, J., Zong, G., and Bi, S., 2010, "An Effective Pseudo-Rigid-Body Method for Beam-Based Compliant Mechanisms," Precis. Eng., **34**(3), pp. 634–639.

[12] Pucheta, M. A., and Cardona, A., 2010, "Design of Bistable Compliant Mechanisms Using Precision-Position and Rigid-Body Replacement Methods," Mech. Mach. Theory, **45**(2), pp. 304–326.

[13] Wang, N., Liang, X., and Zhang, X., 2014, "Pseudo-Rigid-Body Model for Corrugated Cantilever Beam Used in Compliant Mechanisms," Chin. J. Mech. Eng., **27**(1), pp. 122–129.

[14] Hao, G., and Li, H., 2015, "Conceptual Designs of Multi-Degree of Freedom Compliant Parallel Manipulators Composed of Wire-Beam Based Compliant Mechanisms," Proc. Inst. Mech. Eng., Part C: J. Mech. Eng. Sci., **229**(3), pp. 538–555.

[15] Zhu, B., Zhang, X., Zhang, H., Liang, J., Zang, H., Li, H., and Wang, R., 2020, "Design of Compliant Mechanisms Using Continuum Topology Optimization: A Review," Mech. Mach. Theory, **143**, p. 103622.

[16] Yoon, G., Kim, Y., Bendsøe, M. P., and Sigmund, O., 2004, "Hinge-Free Topology Optimization With Embedded Translation-Invariant Differentiable Wavelet Shrinkage," Struct. Multidiscipl. Optim., **27**(3), pp. 139–150.

[17] Kim, J. E., Kim, Y. Y., and Min, S., 2005, "A Note on Hinge-Free Topology Design Using the Special Triangulation of Design Elements," Commun. Numer. Methods Eng., **21**(12), pp. 701–710.

[18] Zhou, H., and Killekar, P. P., 2011, "The Modified Quadrilateral Discretization Model for the Topology Optimization of Compliant Mechanisms," ASME J. Mech. Des., **133**(11), p. 111007.

[19] Saxena, A., 2008, "A Material-Mask Overlay Strategy for Continuum Topology Optimization of Compliant Mechanisms Using Honeycomb Discretization," ASME J. Mech. Des., **130**(8), p. 082304.

[20] Sigmund, O., 2007, "Morphology-Based Black and White Filters for Topology Optimization," Struct. Multidiscipl. Optim., **33**(4), pp. 401–424.

[21] Luo, Z., Chen, L., Yang, J., Zhang, Y., and Abdel-Malek, K., 2005, "Compliant Mechanism Design Using Multi-objective Topology Optimization Scheme of Continuum Structures," Struct. Multidiscipl. Optim., **30**(2), pp. 142–154.

[22] Li, R., and Zhu, B., 2016, "An Augmented Formulation of Distributed Compliant Mechanism Optimization Using a Level Set Method," Adv. Mech. Eng., **8**(8), p. 1687814016664489.

[23] De Leon, D. M., Alexandersen, J., and Sigmund, O., 2015, "Stress-Constrained Topology Optimization for Compliant Mechanism Design," Struct. Multidiscipl. Optim., **52**(5), pp. 929–943.

[24] Xia, Q., and Shi, T., 2015, "Constraints of Distance From Boundary to Skeleton: For the Control of Length Scale in Level Set Based Structural Topology Optimization," Comput. Meth. Appl. Mech. Eng., **295**, pp. 525–542.

[25] Yoon, G. H., Kim, Y. Y., Langelaar, M., and van Keulen, F., 2008, "Theoretical Aspects of the Internal Element Connectivity Parameterization Approach for Topology Optimization," Int. J. Numer. Meth. Eng., **76**(6), pp. 775–797.

[26] Kim, J. H., Choi, Y. H., and Yoon, G. H., 2023, "Development of a Joint Distance Constraint for Optimized Topology and Optimized Connection for Multiple Components," Eng. Optim., **55**(9), pp. 1456–1476.

[27] Yi, B., Yoon, G. H., and Peng, X., 2021, "A Simple Density Filter for the Topology Optimization of Coated Structures," Eng. Optim., **53**(12), pp. 2088–2107.

[28] Zhang, W., Yuan, J., Zhang, J., and Guo, X., 2016, "A New Topology Optimization Approach Based on Moving Morphable Components (MMC) and the Ersatz Material Model," Struct. Multidiscipl. Optim., **53**(6), pp. 1243–1260.

[29] Van Dijk, N. P., Maute, K., Langelaar, M., and Van Keulen, F., 2013, "Level-Set Methods for Structural Topology Optimization: A Review," Struct. Multidiscipl. Optim., **48**(3), pp. 437–472.

[30] Svanberg, K., 1987, "The Method of Moving Asymptotes–A New Method for Structural Optimization," Int. J. Numer. Meth. Eng., **24**(2), pp. 359–373.